

PET image reconstruction with system matrix based on point spread function derived from single photon incidence response*

Fan Xin(樊馨)^{a)c)}, Wang Hai-Peng(王海鹏)^{a)c)}, Yun Ming-Kai(袁明凯)^{a)b)}, Sun Xiao-Li(孙校丽)^{a)c)}, Cao Xue-Xiang(曹学香)^{a)b)}, Liu Shuang-Quan(刘双全)^{a)b)}, Chai Pei(柴培)^{a)b)}, Li Dao-Wu(李道武)^{a)b)}, and Wei Long(魏龙)^{a)b)†}

^{a)} Key Laboratory of Nuclear Analytical Techniques, Institute of High Energy Physics, Chinese Academy of Sciences, Beijing 100049, China

^{b)} Beijing Engineering Research Center of Radiographic Techniques and Equipment, Beijing 100049, China

^{c)} University of Chinese Academy of Sciences, Beijing 100049, China

Abstract

In positron emission tomography (PET) imaging, statistical iterative reconstruction (IR) techniques appear particularly promising since they can provide accurate physical model and geometric system description. The reconstructed image quality mainly depends on the system matrix model which describes the relationship between image space and projection space for the IR method. The system matrix can contain some physics factors of detection such as geometrical component and blurring component. Point spread function (PSF) is generally used to describe the blurring component. This paper proposes an IR method based on the PSF system matrix, which is derived from the single photon incidence response function. More specifically, the gamma photon incidence on a crystal array is simulated by the Monte Carlo (MC) simulation, and then the single photon incidence response functions are obtained. Subsequently, using the single photon incidence response functions, the coincidence blurring factor is acquired according to the physical process of PET coincidence detection. Through weighting the ordinary system matrix response by the

*Project supported by National Natural Science Foundation of China (Grant No Y4811H805C).

† Corresponding author. E-mail: weil@ihep.ac.cn

coincidence blurring factors, the IR system matrix based on the PSF is finally established. Using this system matrix, reconstructed image is produced by OSEM algorithm. The methods could improve image resolution, contrast and increase signal-to-noise ratio obviously, comparing with the IR using ordinary system matrix model. Meanwhile, the single gamma-ray incidence simulated response function only depends on the crystal configuration so that the method could be extended to any PET scanners with the same detector crystal configuration.

Key words: PSF, single photon incidence, system matrix, PET

PACS:87.57.nf, 87.57.uk, 87.57.C-

1. Introduction

Positron emission tomography (PET) is a nuclear medical imaging technique and provides important information for disease diagnosis, therapeutic effect assessment and new drug development.^[1] The PET system detects pairs of back to back gamma photons emitted indirectly from a positron-emitting radionuclide, which is injected into the living body on a biologically active tracer. The image of tracer concentration within the living body can be acquired by image reconstruction methods such as analytic reconstruction^[2] and statistical iterative reconstruction (IR).^[3] The quality of PET imaging is vital for disease diagnosis and evaluation of treatment. It includes image resolution, contrast, signal-to-noise ratio and so on.^[4] The image resolution which is crucial for diagnosis of early stage tumor mainly depends on several factors such as the size of detector, the photon non-collinearity, the positron range and inter-crystal penetration.^[5,6,7,8] The size of detector may not be changed for an existing system. Among the other physical and geometric factors, crystal penetration will lead to depth-of-interaction (DOI) blurring. The image spatial resolution degradation and misposition turn more serious as the DOI blurring increasing.^[9] These physical and geometric factors can be accurately modeled by the system matrix in IR reconstruction.^[8]

Traditionally, the system matrix can be divided into some component such as

geometrical component, blurring component and so on. Point spread function(PSF) is generally used to describe the blurring component. PSF can be modeled by the analytic methods, ^[10-12] the Monte Carlo (MC) simulation methods ^[13-15] and the experimental methods ^[16-22]. It's a huge work to get the spatially variant PSFs^[23] of all the voxels in the experiment methods,^[19] while purely analytic methods is less accurate than the other methods.^{[19][20]} Several studies proposed some methods which firstly obtained a few specific PSFs by the experimental measurements or MC simulations and then used specific models(for example Gaussian function model^[19] or iterative algorithm^[22]) to estimate the PSF of all voxels based on the system symmetry.^{[19][20][22]} Thus, the experimental time is reduced dramatically. However, it's improper for an accuracy system model to only model the radial blurring but ignore the azimuthal blurring^{[19][20]} as in most of these methods. Moreover, it is tedious work that more than one experiment or simulation needs to be implemented for different geometrical structures of PET scanners in these methods.^{[19][20]}

In this paper, we propose an advanced method which obtains the PSF information based on the single gamma photon incidence response function. This method can be extend to any PET scanners with the same crystal configuration owing to this generalized response function. This single photon incidence response function on the detector array is obtained by MC simulation. Then according to this response function, the blurring of coincidence detection is acquired. Weighting the ordinary system matrix response by this blurring factor, 2-D PSFs of all the voxels are obtained according to relevant system geometry. Finally, the raw data of 3D acquisition is reconstructed using PSF blurring system matrix based on OSEM^[3] after Fourier rebin^[24] to produce the image. We verifies our method in the MC simulation imaging experiments and the whole body PET imaging experiments (supported by in-beam whole body PET, Institute of High Energy Physics Chinese Academy of Sciences). The results show that this method could improve the image spatial resolution obviously comparing with the ordinary OSEM algorithm.^[3] And the contrast and signal-to-noise ratio are also verified improved in the MC simulation imaging experiments.

2. Theory

In the IR methods, the system matrix describes the relationship between projection space and image space. It could be expressed as:

$$p_j = \sum_i a_{ij} f_i \quad (1)$$

where p_j is the true value of the projection data for a line of response (LOR) (or the coincidence crystal pair) decided by the detector pair j . f_i is the value of the image space at voxel i . a_{ij} is the probability of detecting a coincidence from voxel i at detector pair j .^[19] We define A representing the matrix of a_{ij} . So A is the system matrix which contains the geometrical projection matrix A_{geom} , the blurring matrix A_{blur} , the attenuation factor A_{atten} , the detector sensitivity factor A_{sens} and the positron range factor $A_{positron}$, which can be expressed as:

$$A = A_{sens} A_{atten} A_{blur} A_{geom} A_{positron} \quad (2)$$

Among these factors, the positron range factor $A_{positron}$ is relatively smaller and can be ignored for ^{18}F .^[25] The attenuation factor A_{atten} can be provided by an extra CT scan^[26] and the detector sensitivity factor A_{sens} can be acquired by measuring a uniform cylindrical source.^[27] The remaining factors are the geometrical matrix and the blurring matrix.^[28] The geometrical matrix can be calculated accurately by some geometrical methods such as the line integral model,^[29] the tube model^[30] and the solid angle model.^{[31][19]} However, owing to the complicate response, blurring matrix is always difficult to be acquired accurately. It should include the physical effects such as the crystal penetration, and the photon non-collinearity^[5,6,7,8] which would result in the degradation of reconstructed image quality as mentioned before.

3. PSF modeling method

3.1. Monte Carlo simulation for single photon incidence response function

In PET scanner, the blurring effect mainly comes from DOI blurring. DOI blurring results from crystal penetration which is caused by non-normal incidence of gamma-ray.^[9] The bigger the angle of incidence is, the more serious DOI blurring is.^[32] Fig. 1 displays three different incidence angle of gamma-ray to the detector plane. When incidence is vertical, there are few crystals being penetrated [Fig.1(a)]. When incidence angle is non-normal, the gamma-ray may penetrate a few adjacent crystals [Fig.1(a) and Fig.1(b)]. The response of gamma-ray in the penetrated crystals is mainly decided by incidence angle.^[32] In Fig.1(b), the gamma-ray penetrates two crystals but in Fig.1(c) the gamma-ray whose incidence angle is larger penetrates three. Generally, PET scanner is not a standard circle but a regular polygon composed of a certain number of uniform blocks (the crystal array). Theoretically if we get response of all incidence angle of the single gamma-ray photon for one block, we can get all the response of a PET system with a certain geometrical shape no matter what the geometrical shape is, because its blocks are uniform.

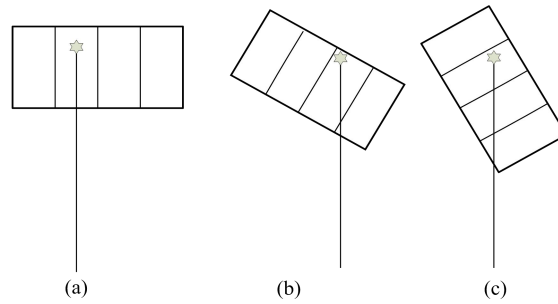


Fig.1. Three different incidence patterns of gamma-ray. (a) vertical incidence of gamma-ray. (b) oblique incidence of gamma-ray. (c) larger angle of incidence of gamma-ray compared to (b)

In fact, we only need to get incidence angles in enough range which includes all incidence angles of the devices. Here, we define the complement angle of the ordinary incidence angle as incidence angle in this paper for the convenience of calculation (for example θ of Fig.2). We calculated the geometry of sixty-four polygon scanner

with each block having 11×11 LYSO crystals and the forty-eight polygon scanner with each block having 15×15 LYSO crystals. And the crystal size are both $3.5 \text{ mm} \times 3.5 \text{ mm} \times 15 \text{ mm}$. The gap between every two block is 4 mm for the former one and 3.4 mm for the latter one. Incidence angle range of the former one is $42.7^\circ - 90.0^\circ$ degree with 353 bins of every 702° angle. And the latter one is $41.7^\circ - 90.0^\circ$ degree with 361 bins of every 720° angle. So we only need to get incidence angle from 30° to 90° degree to satisfy incidence angle of this two scanners.

We simulated the response mentioned above by the Geant4 Application for Emission Tomography (GATE) software based on the MC methods. In the simulation, 15×1 LYSO crystal array was set with a lead collimator to obtain the different angle of incidence [Fig.2]. The crystal array was rotated to produce a certain angle with the lead collimator assuring the direction of single incidence. The middle crystal was the incident one and we obtained the response based on probabilistic method [Fig.3]. As in Fig.3, in one angle's response, assuming N events have been recorded totally [Fig.3], there are n_1 , n_2 and n_3 events recorded in crystal 1, crystal 2, and crystal 3 respectively, so the corresponding probability of response are n_1/N , n_2/N and n_3/N respectively. In addition, we try to take incidence angle-step for 5° from 30° degree to 90° degree for the first attempt.

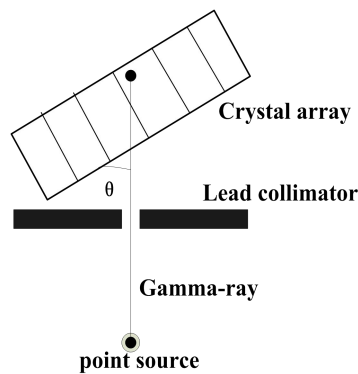


Fig.2. The simulation setting of the single gamma-ray photon incident

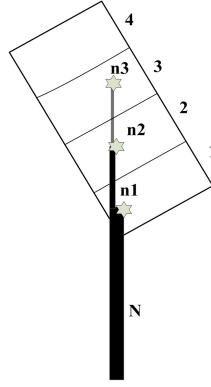


Fig.3. Probabilistic method of getting the response of single gamma-ray photon incident

Fig. 4 displays a part of the results we simulated. Actually, we only used a few response of the penetrated crystals which were penetrated firstly in the following calculation to save computational time because of the low probability of the latter penetrated crystals. The sum of these response accounted for over 80% of total response.[Fig. 4]. Fig.4 (a) and (c) show the original response. (b) and (d) show the normalized 80% of response. We can see that the gamma-ray of 60 degree incident angle has penetrated more crystals than the gamma-ray of the 90 degree angle (vertical incidence) as same as most of former studies.

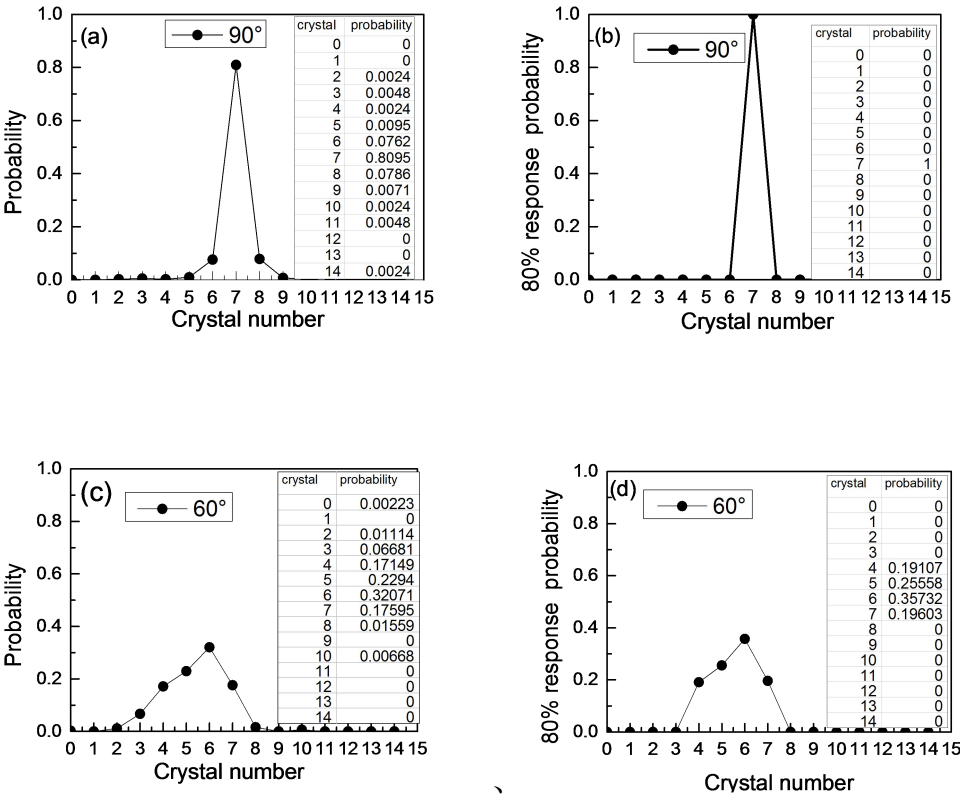


Fig.4. Single gamma-ray response function simulated by MC methods. (a) and (c) are the original response of 90,60 degrees incidence angle respectively. (b) and (d) are the 80% of the response which have normalized of 90,60 degrees incidence angle respectively. The inset shows the corresponding response table.

3.2. Coincidence for PSF-based system matrix and reconstruction of PSF-OSEM

In PET scanner, the data is acquired from coincidental response of a pair of crystals. We coincided two back to back single gamma-ray photon response using the single photon incidence response function from 3.1[Fig.5]. When the signals are acquired from the recorded events of a pair of crystals, responses of two crystals are generated simultaneously so that the gamma-ray in penetrated crystals in two sides would be recorded as a coincidence event for every two crystal in these pixelate-detectors^[32]. As in Fig.5, solid line represents incidence coincidence LOR, and incidence angle of corresponding crystal b and g are θ_1 and θ_2 respectively. On the θ_1 side, penetrated crystals are b and c, while on the other side are g, h and i. Thus, the blurring of coincidence LORs which are decided by (b, g), (b, h), (b, i), (c, g), (d, h) and (c, i) crystal pairs are obtained. The corresponding response probability is the product of probability of the two sides penetrated crystals in the single photon response of corresponding incidence angles.^[32] In Fig.5, the corresponding incidence angles are θ_1 and θ_2 . In Table 1, crystal a is the incident crystal. The adjacent crystal to a is a-i and a+i ($i=1,2,3,4$). If the probability is 0, the corresponding crystal is not penetrated. So in incidence of angle θ_1 , the response probability of crystal b and c are p_1 and p_{11} respectively in Table 1. Similarly, the response probability of crystal g, h and i are p_2 , p_{21} , p_{22} respectively. Table 2 shows the coincident results of LOR blurring response. Obviously, the LOR blurring response contains the radial and azimuthal blurring in transverse plane.^[24]

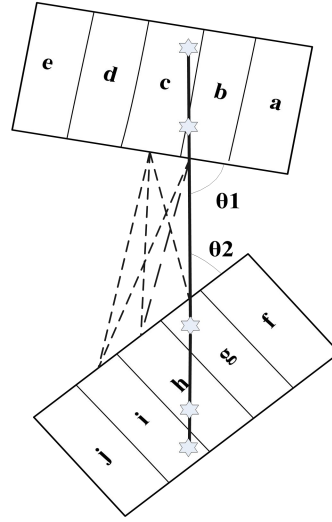


Fig.5. Coincidence process. Solid line is the incident coincidence LOR and dash line is the blurring LOR.

Table 1. Single gamma-ray photon response probability of incidence angle θ_1, θ_2 .

Incident angle	Crystal number								
	a-4	a-3	a-2	a-1	a	a+1	a+2	a+3	a+4
θ_1	0	0	0	p11	p1	0	0	0	0
θ_2	0	0	p22	p21	p2	0	0	0	0

Table 2. The coincident result of LOR blurring response.

Coincident event	Response probability
Event (b,g)	$p1 \times p2$
Event (b,h)	$p1 \times p21$
Event (b,i)	$p1 \times p22$
Event (c,g)	$p11 \times p2$
Event (b,h)	$p11 \times p21$
Event (b,i)	$p11 \times p22$

PET scanner often has a symmetrical geometry, so that we only need to calculate a certain number of LOR blurring response to get all the blurring response of LORs by making use of the symmetry of the system geometry.^[22]

Fig.6 shows two different radial positions of 0 angle sinogram (a organizational form of LOR) blurring. The scanner geometry we use is sixty-four polygon as

mentioned before. We can see that the bins of both two positions generated the radial blurring and the azimuthal blurring. (a) and (b) represent the furthest bin off the center of the FOV. The radial offset is very serious so that the location of the point source has a large error in the no-PSF reconstruction. And the azimuthal response only has some slightly blurring not large offset.^[19] (c) and (d) is response of center bin's and there's no serious blurring.

Fig.7 displays the comparison between two point responses in sinograms (PSF) gained by our method and MC simulation of GATE software. The geometry of scanner is the same as in Fig.6. Fig.7(a), (b) and (c) show the point response of center point. And the simulated point response [Fig.7 (a)], the blurring point response using our method [Fig.7(b)] and the no-blurring point response [Fig.7(c)] are similar because of the weak blurring[Fig.6(c)]. But at the edge of the FOV [Fig7. (d), (f) and (e)], the edge bins (the top of sinogram and the bottom of sinogram) begin to blur or spread in the simulated point response. The blurring point response [Fig.7 (e)] can describe this blurring spread accurately. But the no-blurring point response [Fig.7 (f)] does not contain the blurring spread.

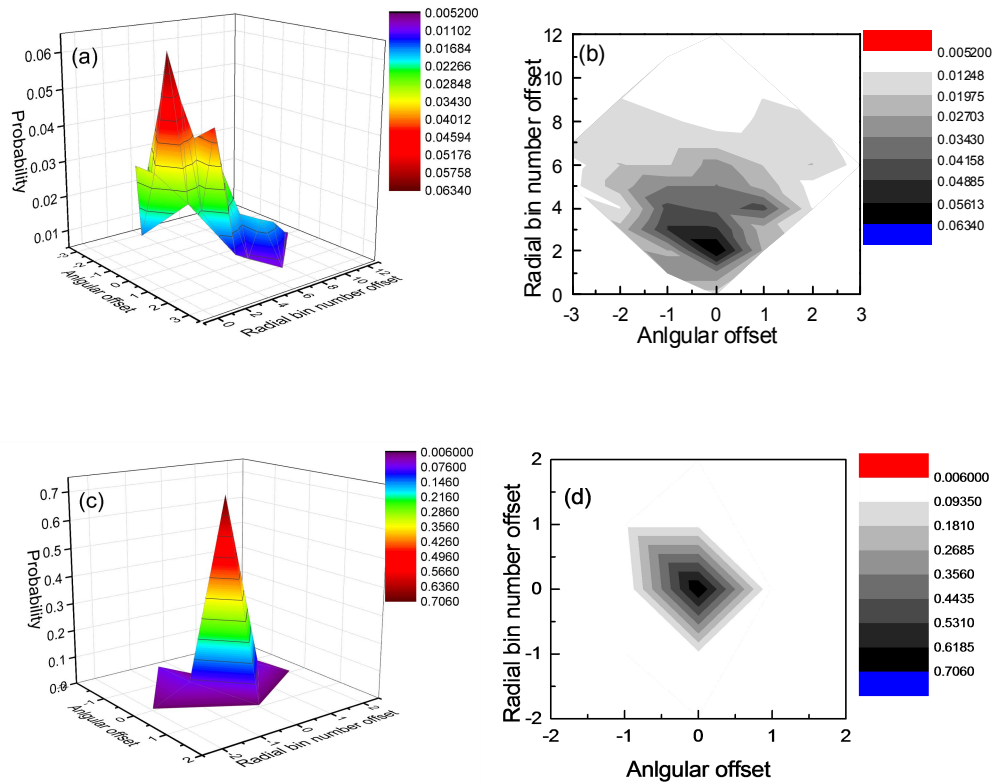


Fig.6. (color online) The bin's blurring response of LOR at two different position of the 0 degree sinogram. We take 704 angles of every 87 slice and 353 radial bins in each angle for scanner. (a) and (b) represent the NO.1 bin. (c) and (d) represent the NO.176 bin (the center bin). (a) and (c) present the 3D view of the response. (b) and (d) present the plane view of the response.

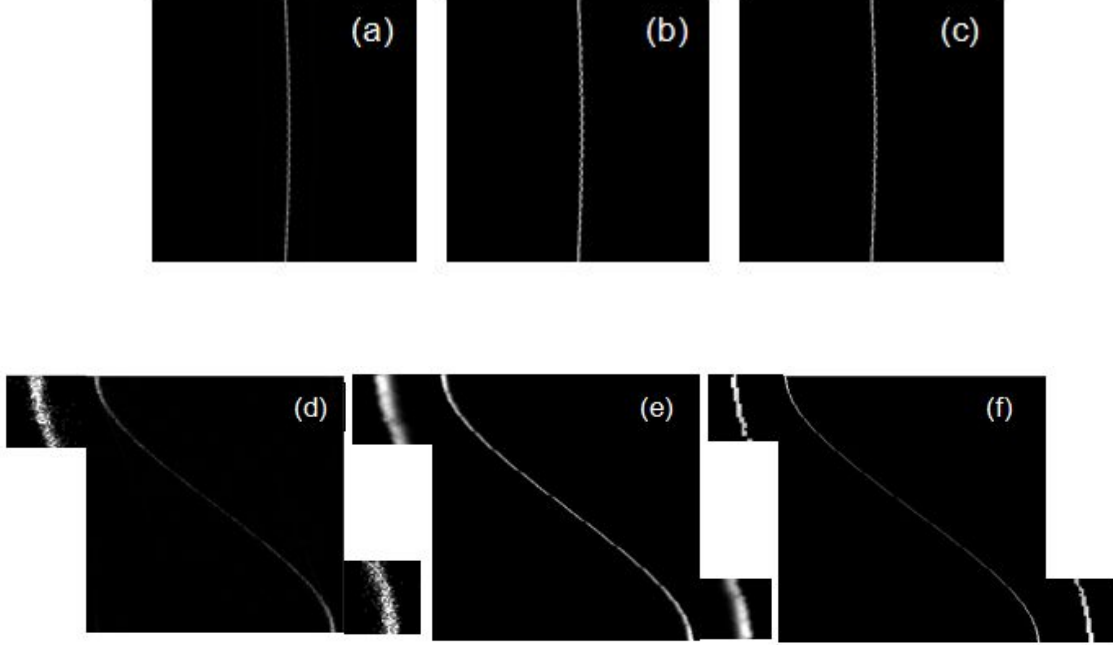


Fig.7. The point response of two points of three methods in sinogram. Diameter of the points are 0.5 mm. (a) and (d) are the MC simulation response by GATE software. (b) and (e) are blurring results using our method. (c) and (f) are the no-blurring results. (a), (b) and (c) show the point response of point placed in the center of the FOV. (d), (e) and (f) show the point response of point placed in the 300 mm off the center of the FOV.

At last, we plus the PSF factor to the geometrical system matrix for the forward projection and the back projection by real-time computing to reduce the memory consumption. In addition, PSF-OSEM method consume more computational time compared to OSEM method ^[28]for the additive spread.

4. Results

Our goal of this PSF reconstruction is to improve the image quality and save resource. We only need to simulate the response of a certain number of single photon

of gamma-ray but not PSFs of all the voxels in the FOV. Our data comes from both experiment in the system of the MC simulation of GATE software and the experiment in our whole body PET scanner. The scanner systems are both sixty-four polygon with 64×4 blocks (4 blocks in axial direction). Each block equips with 11×11 LYSO crystals as we mentioned before. The size of crystal is $3.5 \text{ mm} \times 3.5 \text{ mm} \times 15 \text{ mm}$. The gap between every two block is 4 mm. The data were acquired with a 361 keV–661 keV energy window and 6 ns timing window. We binned the emission data to a $704 \times 353 \times 87$ sinogram matrix after Fourier rebin. There are 704 angles for every 87 slice and 353 radial bins for each angle.

4.1. Image resolution

The single point resolution is improved in the PSF-OSEM method. Fig.8 shows the reconstructed image of point array which was simulated from the system of MC simulation. The diameter of each point is 0.5 mm. The closest point is 140 mm off the center of FOV and the furthest point is 300 mm off the center of FOV. The distance between every two point is 20 mm in both radial and tangential direction. We take 8 subsets and 10 iterations and 1 mm image pixel for the reconstruction without smoothing. We can see in Fig.8(a) that the further the point is, the worse the radial resolution is in the image from OSEM reconstruction.^[3] But the radial resolution is uniform in the PSF-OSEM reconstruction. This conclusion is also confirmed in the profile curve of points of the middle row in Fig.8(b). The points reconstructed in OSEM method^[3] show up the wider full width at half maximum (FWHM) in curve as well as the larger position offset to the FOV center direction which may result in locating error.

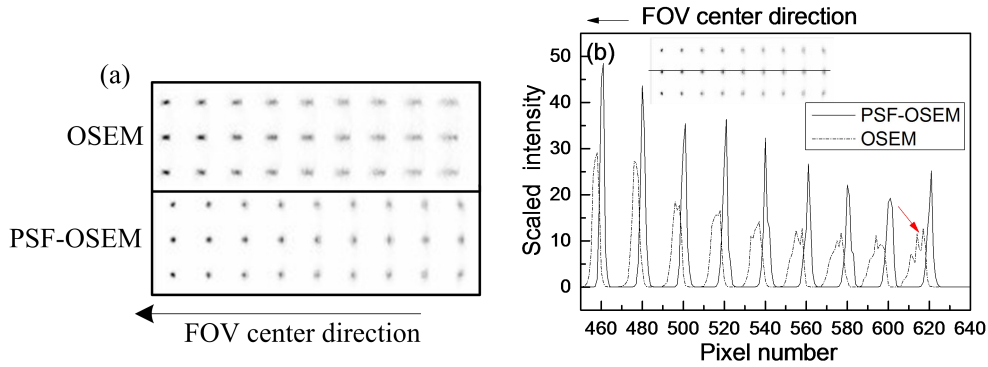


Fig.8. (color online) The reconstructed image and the middle line profile of the point array generated by MC simulation. The diameter of each point is 0.5 mm. The closest point is 140 mm off the center of FOV and the furthest point is 300 mm off the center of FOV. The distance between every two point is 20 mm in both radial and tangential direction. (a) is the reconstructed image of point array. (b) is the profile of middle line points.

Fig.9(a) shows the radial resolution versus location whose points are generated from the system of the MC simulation as well. The points are simulated singly according to the NEMA Standards Publication.^[4] The diameter of the points are also 0.5 mm. Every point image is acquired by 8 subsets and 2 iterations without smoothing both in the two algorithm. The pixel size is 0.5 mm for the first four points and 1mm for the last three points according to NEMA Standards Publication.^[4] The curve shows that the degradation of the radial resolution increase as the radial offset increasing in the OSEM reconstruction^[3] because of the DOI effects. The best radial resolution is 2.46 mm, and the worst resolution is 6.96 mm. In the PSF-OSEM, the radial resolution is much better in the degradation. The best radial resolution is 2.42 mm and the worst one is 4.41mm. Fig.9(b) shows the tangential resolution versus location which is similar in the two methods. But notice the point of the 300 mm radial offset in the OSEM reconstruction^[3] that the tangential resolution suddenly become lower. This is because the furthest point has turned long and narrow even split into two or three points because of DOI effects. The profile curve [Fig.8(b)] of the point on the pixel 620 (300 mm radial offset) shows the split and the Fig.9(d) shows the narrow tangential resolution. Fig.9(c) presents the radial position error versus the location. Obviously, the points reconstructed by OSEM reconstruction^[28] have quite

larger error in radial position and all the points shift to the center of FOV. The biggest shift is 6mm. Notice the points at 150mm radial offset and the 300 mm radial offset reconstructed by OSEM algorithm^[3] that they both have saltus as well as the sudden slight decrease of the tangential resolution. That is because both two positions are in the gap between two blocks in the direction perpendicular to the radial direction. So the DOI effects are serious. Points reconstructed by the PSF-OSEM algorithm don't have these saltus in comparison. Table 3 shows the percent of the image resolution improved. We define this percent as follow:

The percent of radial resolution improved turned larger from the point of the 150 mm radial offset. The biggest one is up to 45.2%. All the points' percents except the last one (in the position of 300 mm) of tangential resolution improved are slightly fluctuations and it means the tangential resolution of these points reconstructed by both algorithms are similar[Fig.9(b)]. But the abnormal percent of the point in the position of 300 mm has the same reason with Fig.9(b).

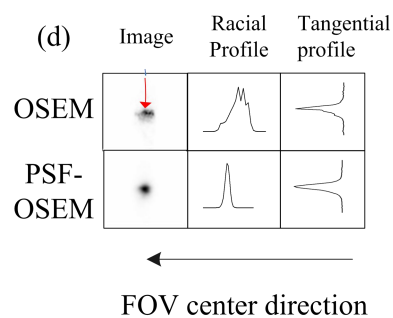
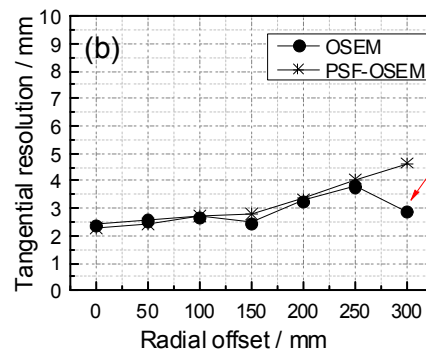


Fig.9. (color online) Radial resolution and tangential resolution and the radial position error versus location of the single points generated from the system of the MC simulation. (a) is the radial resolution curve versus location. (b) is the tangential resolution curve versus the location. (c) is the radial position error versus the location. (d) is the reconstructed image of the 300 mm point(the furthest point).

Table 3. The percent of the image resolution improved for simulated dada							
Improved item	Radial offset (mm)						
	0	50	100	150	200	250	300
Radial resolution	1.9%	22.35%	3.2%	21.8%	35.9%	45.2%	36.6%
Tangential resolution	4.8%	5.9%	-1.1%	-12.4%	-2.5%	-6.4%	<u>-60.8%</u>

Fig.10 and Fig.11 show resolution condition of our PET data. The three rob sources in Fig.10 are filled with the ^{68}Ge and the activity concentration of the top rob is 3 μCi and the other two robs are 0.5 μCi . The diameter of each rod is 3 mm. The center of triangle composed by the three robs is at the position of 282 mm off the center of the FOV. We also make 8 subsets and 10 iterations and 1 mm image pixel for the reconstruction without smoothing. Fig.11 (a), (b) and (c) are the image resolution curve and the radial position error versus the position of the single points respectively. The single point is filled with 25 μCi ^{22}Na and the diameter is 0.5 mm and the position is configured also by the spatial resolution of NEMA Standards Publication^[4]. Every point image is acquired by 8 subsets and 2 iterations without smoothing both in the two algorithm. The pixel size is also 0.5 mm for the first four points and 1 mm for the last three points according to NEMA Standards Publication.^[4] We can see the same conclusion in the experimental data and the simulated data. The smallest and biggest radial resolution are 2.39 mm and 4.24 mm respectively in PSF-OSEM. And the corresponding radial resolution are 2.98 mm and 7.14 mm respectively in OSEM. Table 4 shows the percent of the image resolution improved for our PET dada. Radial and tangential resolution are both improved except the last point because of DOI effect.

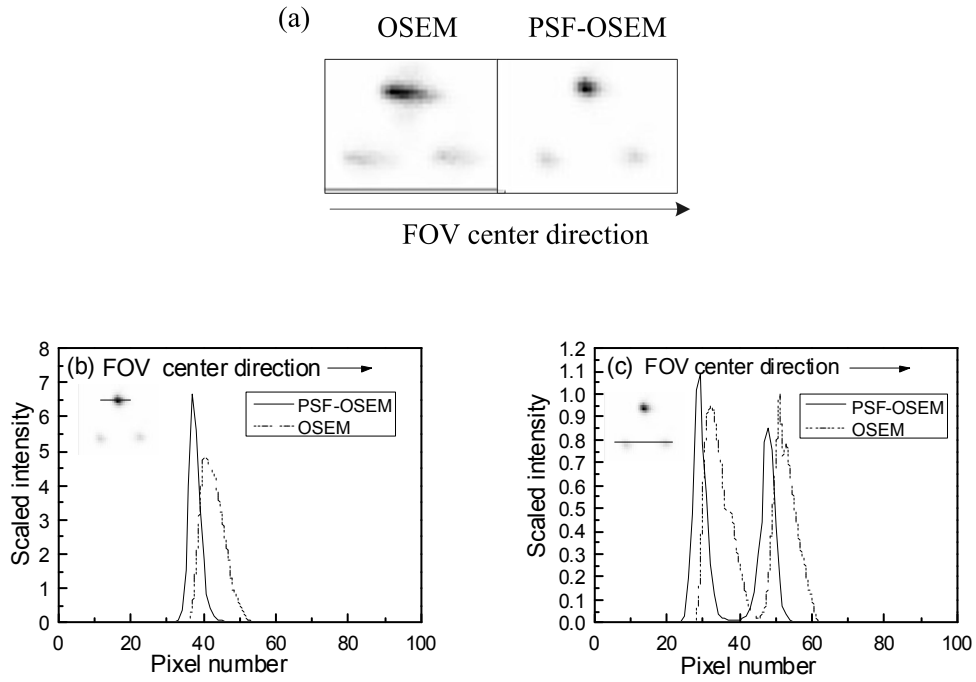
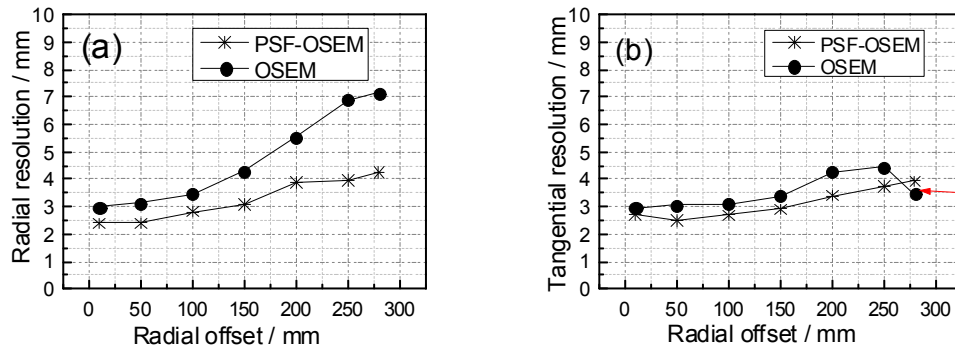


Fig.10. The center slice of the reconstructed image of the three rob source data acquired from our PET scanner. The three rob sources are fill with the ^{68}Ge and the activity concentration of the top rob is $3\ \mu\text{Ci}$ and the other two robs are $0.5\ \mu\text{Ci}$. The diameter of each rod is 3 mm. The center of triangle composed by the three robs is at the position of 282 mm off the center of the FOV. (a) is the center slice of reconstructed image of the three robs. (b) is the profile of the top rob of the center slice. (c) is the profile of the other two robs of center slice.



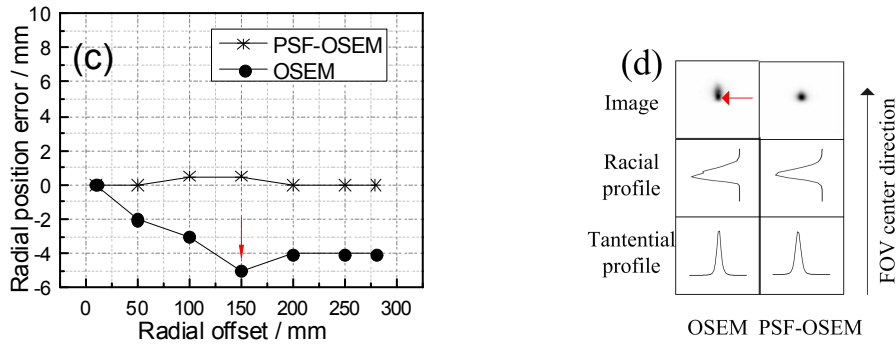


Fig.11. (color online) Radial resolution and tangential resolution and the radial position error versus location of the single points data acquired from our PET scanner. The single point is fill with 25 μCi ^{22}Na and the diameter is 0.5 mm. (a) is the radial resolution curve versus location. (b) is the tangential resolution curve versus the location. (c) is the radial position error versus the location. (d) is the reconstructed image of the 280 mm point (the furthest point).

Table 4. The percent of the image resolution improved for our PET dada

Improved item	Radial offset (mm)						
	10	50	100	150	200	250	280
Radial resolution	19.3%	23.8%	18.8%	27.9%	29.8%	42.4%	40.6%
Tangential resolution	7.6%	20%	13.8%	13.8%	20.4%	15.9%	<u>-13.4%</u>

4.2. The contrast and noise ratio

We simulated the sphere phantom in the system of MC simulation. The ratio of activity concentration of hot spheres and the background is 8:1. The diameter of hot spheres are 10 mm, 13 mm, 17 mm, 22 mm respectively. Fig.12 shows a transverse image of the center slice of the sphere and a profile of center row of the two smallest spheres. The phantom image is acquired by 8 subsets and 5 iterations without smoothing after corrections for random, normalization, scatter and attention. The image pixel size is 1 mm. Fig.13 presents the curve of the merit of contrast and signal to noise ratio. We choose ± 1 , ± 2 slices offsetting center slice together with the center slice and choose 12 background regions of interest (ROI) for each slice. So there are

60 background ROIs totally.^[31] Fig.13 shows the contrast recovery curve of the hot spheres and the percent background variability. Table 4 shows the percent of hot sphere contrast recovery and percent background variability improved. The contrast recovery is improved obviously. The variability of background is improved greatly in the smaller size spheres.

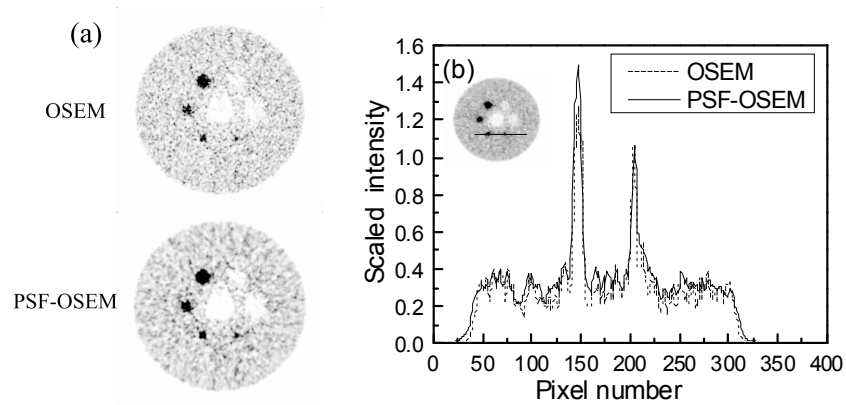
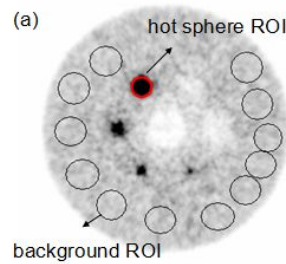


Fig.12. Transverse image of the center slice of the sphere phantom and a profile of center row of the two smallest sphere which simulated by the system of MC simulation. The ratio of activity concentration of hot spheres and the background is 8:1. The hot spheres' diameter are 10 mm, 13 mm, 17 mm and 22 mm respectively. (a) is the reconstructed image. (b) is the profile of center row of the two smallest sphere.



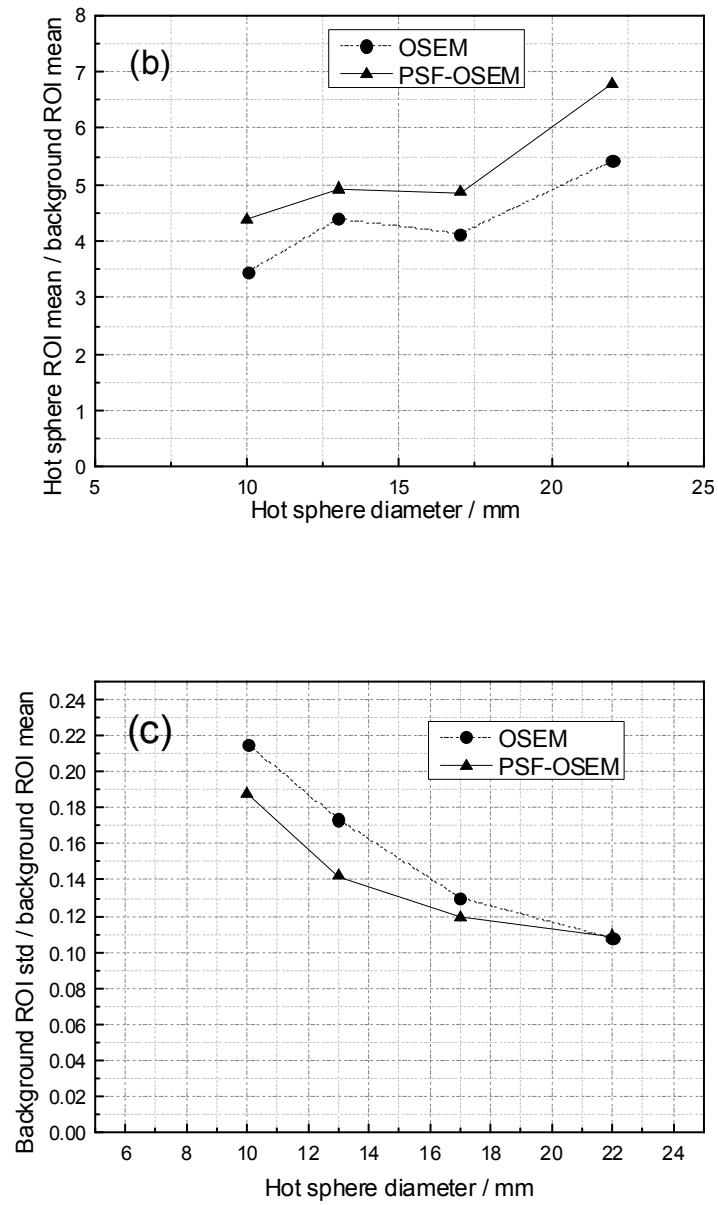


Fig.13. (color online) The curve of the merit of contrast and signal-noise ratio. (a) is the ROI chosen method. (b) is the hot sphere contrast recovery (hot sphere ROI mean divide the background ROI mean) curve versus the sphere diameter. (c) is the percent background variability(background ROI std divide the background ROI mean) versus the sphere diameter.

Table 5. The percent of hot sphere contrast recovery and percent background variability improved

Improved Item	Sphere diameter(mm)			
	10	13	17	22
Hot sphere contrast recovery	26%	11.9%	10.6%	25%
Percent background variability	12.9%	18.1%	8.3%	0%

5. Conclusions and discussions

In PET scanner system, the image quality is degenerated by DOI blurring. Our methods based on the single photon incidence can get this DOI blurring. This method improves the resolution, contrast, and signal-noise ratio obviously. In addition, the single photon response function depends on the crystal specification but not the system geometry. With this advantage, we only need to change the calculational coincidence process to adapt to the geometry of a certain system. However, there are also several problems need to be discussed.

5.1. The single photon incidence angle step

In our paper, we only choose the step of five degree and the resolution improved inspiringly. If we resize the step to a proper value that matches with the response, the quality of the image may be improved more obviously. In this paper, we simulated the response by uniform step. But in fact the response of single photon penetrating crystals may be nonuniform. The distribution that single photon penetrates crystals is our future work.

5.2. Convergence and computational time

Commonly, PSF reconstruction converges slower than the non-PSF because PSF contains a lot blurring information. And the variational PSF decides the variational convergence.^[23] Fig.14 shows the convergence visually. The points far away from the

center of FOV converge slower than the center ones. We must consider to add some acceleration algorithm (for example the GPU acceleration algorithm) in PSF reconstruction to solve this problem.

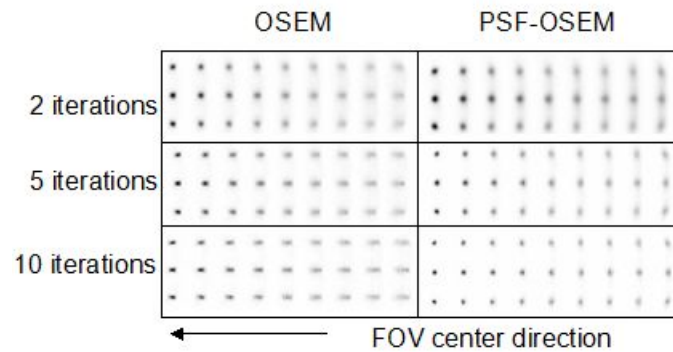


Fig .14. The convergence comparison of the point array in Fig.8 for 2,5,10 iterations.

References

- [1] S.S.Gambhir, J.Czermin, J.schwimmer, D.H.Silverman, R.E.Coleman and M. E. Phelps
2001 *J. Nucl. Med* 42 1S-93S
- [2] Natterer F, Wuebbeling F. 2001 *Mathematical methods in image reconstruction*.SIAM
Monographs on Mathematical Modeling and Computation
- [3] H. Hudson and R. Larkin 1994 *IEEE Trans. Med. Imaging* 13 601
- [4] M. E. Daube-Witherspoon, J. S. Karp and M. E. Casey 2002 *J. Nucl. Med.* 43 1398
- [5] O.Mawlawi and D. W. Townsend 2009 *Eur J. Nucl. Med. Mol. Imaging* 36 S15
- [6] U.Nestle, W.Weber, M.Hentschel and A.L.Grosu 2009 *Phys. Med. Biol.* 54 R1
- [7] T. Pan and O. Mawlawi 2008 *Med. Phys.* 35 4955
- [8] David B. Wiant, Jacob A. Gersh, Marcus C. Bennett and J.Daniel Bourland 2009 *Nuclear
Science Symposium Conference Record* Oct. 24 - Nov. 1 2009 Orlando FL p.3758
- [9] Chien-Min Kao, Yun Dong, Qingguo Xie and Chin-Tu Chen 2008 *IEEE Trans.
Med.Imaging* May
- [10] R. Lecomte, D. Schmitt and G. Lamoureux 1984 *IEEE Trans. Nucl. Sci.* NS-31 556
- [11] Z. Liang 1994 *IEEE Trans. Med. Imaging* 13 314

- [12] A. Rahmim, J. Tang, M. A. Lodge, S. Lashkari, M. R. Ay, R. Lautamaki, B. M. W. Tsui, and F. M. Bengel 2008 *Phys. Med. Biol.* 53 5947
- [13] A. M. Alessio, P. E. Kinahan, and T. K. Lewellen 2006 *IEEE Trans. Med. Imaging* 25 828837
- [14] E. U. Mumcuoglu, R. M. Leahy, S. R. Cherry, and E. Hoffman 1996 *Nuclear Science Symposium, 1996. Conference Record., 1996 IEEE* Nov.2-9 1996 Anaheim CA 3 p.1569
- [15] J. Qi, R. M. Leahy, S. R. Cherry, A. Chatziioannou and T. H. Farquhar 1998 *Phys. Med. Biol.* 43 1001
- [16] A. M. Alessio and P. E. Kinahan 2008 *5th IEEE International symposium on biomedical imaging: From nano to macro* May 14-17 2008 Paris p.1315
- [17] E. D. Bernardi, F. Zito and G. Baselli 2007 *Engineering in Medicine and Biology Society, 2007. EMBS 2007. 29th Annual International Conference of the IEEE* Aug 22-26 2007 Lyon p. 6547
- [18] E. D. Bernardi, F. Zito, L. Michelutti, L. Mainardi, P. Gerundini, and G. Baselli *Engineering in Medicine and Biology Society, 2003. EMBS 2003. 25th Annual International Conference of the IEEE* Sept.17-21 2003 1 p. 975.
- [19] L. Fin, P. Bailly, J. Daouk and M.-E. Meyer 2009 *Med. Phys.* 36 3072
- [20] V. Y. Panin, F. Kehren, C. Michel and M. Casey 2006 *IEEE Trans. Med. Imaging* 25 907
- [21] V. Y. Panin, F. Kehren, H. Rothfuss, D. Hu, C. Michel and M. E. Casey 2006 *IEEE Trans. Nucl. Sci.* 53 152
- [22] M. S. Tohme and J. Qi 2009 *Phys. Med. Biol.* 4 3709
- [23] Adam M. Alessio*, Charles W. Stearns, Senior, Shan Tong, Steven G. Ross, Steve , Alex Ganin and Paul E. Kinahan 2010 *IEEE Trans. Med. Imaging* 29 938
- [24] M. Defrise, P. Kinahan, D. Townsend, C. Michel, M. Sibomana, and D. Newport 1997 *IEEE Trans. Med. Imaging* 16 145
- [25] J. Qi, R. Leahy, S. R. Cherry, A. Chatziioannou and T. Farquhar 1998 *Phys. Med. Bio.* 43 1001
- [26] Wang L, Wu L W, Wei L, Gao J, Sun C L Chai P and Li D W 2014 *Chin. Phys. B* 23 2027802

- [27] R. D. Badawi, M. Lodge and P. K. Marsden 1998 *Phys. Med. Bio.* 43 189
- [28] M. S. Tohme 2011 Iterative Image Reconstruction for Positron Emission Tomography Based on Measured Detector Response Function Tomography Based on Measured Detector Response Function (Ph.D. dissertation) (California :University of California)
- [29] P. M. Joseph 1982 *IEEE Trans.Med. Imaging* MI-1 192
- [30] C. Johnson, Y. Yan, R. Carson, R. Martino and M. Daube-Witherspoon 1995 *IEEE Trans. Nuclear Science* 42 1223
- [31] C. Chen, S. Lee and Z. Cho 1991 *IEEE Trans. Med. Imaging* 10 513
- [32] Sophie Leonard 2005 Spatial resolution Study of PET Detector Modules Based on LSO Crystals and Avalanche Photodiode Arrays (Ph.D. dissertation) (Brussel:Vrije Universiteit Brussel)